



A combined experimental and theoretical study of surface film formation: Effect of oxygen on the reduction mechanism of propylene carbonate



Atetegeb Meazah Haregewoin ^a, Ermias Girma Legesse ^a, Jyh-Chiang Jiang ^a,
Fu-Ming Wang ^b, Bing-Joe Hwang ^a, Shawn D. Lin ^{a,*}

^a Department of Chemical Engineering, National Taiwan University of Science and Technology, Taipei 106, Taiwan, ROC

^b Graduate Institute of Engineering, National Taiwan University of Science and Technology, Taipei, Taiwan, ROC

HIGHLIGHTS

- Reductive decomposition of PC due to O₂ is explained by using experimental and theoretical data.
- PC decomposes to (PC)₂LiOC(O)OCH(CH₃)CH₂OLi(PC) and Li₂O due to the superoxide radical.
- Li₂CO₃-(PC)₃, (R-OCO₂-Li(PC)₂)₂, where R = -CHCH₂CH₃ are formed due to reduction of PC.

ARTICLE INFO

Article history:

Received 1 November 2012

Received in revised form

14 December 2012

Accepted 3 January 2013

Available online 13 January 2013

Keywords:

Lithium-ion battery

Propylene carbonate

Reductive decomposition

Solid electrolyte interphase

ABSTRACT

Combining experimental and computational techniques can provide a better understanding of surface film formation processes that occur in the lithium-ion battery. In this paper, we show that this joint approach can provide a mechanistic understanding of the effect of oxygen in the reduction of propylene carbonate (PC). We perform FTIR analysis, inside a glove box, after conducting linear sweep voltammetry (LSV) from an open-circuit voltage (OCV) to selected potential regions; subtraction between two successive IR spectra has been made to identify the reduction products formed within each potential range. FTIR analysis in the potential range from OCV to -0.1 V, in conjunction with density functional theory (DFT) calculations, confirm the formation of solvated Li₂CO₃ and (PC)₂LiOC(O)OCH(CH₃)CH₂OLi(PC) due to PC reduction. Our experimental results and DFT calculations suggest that in the potential range from OCV to 1.6 V, PC, in the presence of O₂, can easily decompose by the superoxide ion through a nucleophilic attack at the ethereal carbon atom.

© 2013 Elsevier B.V. All rights reserved.

1. Introduction

The need for lighter, thinner, shorter, and smaller products makes the lithium-ion batteries a popular power source for applications such as mobile phones, laptop computers, digital cameras, electrical vehicles, and hybrid electrical vehicles. A typical lithium-ion battery incorporates three major components: a cathode, an anode, and a non-aqueous organic electrolyte. The electrolyte consists of conducting lithium salts such as LiClO₄, LiAsF₆, LiBF₄, or LiPF₆ dissolved in non-aqueous solvents, mainly comprising cyclic and acyclic carbonates such as ethylene carbonate (EC), propylene

carbonate (PC), diethyl carbonate (DEC), dimethyl carbonate (DMC), or ethyl methyl carbonate (EMC) [1].

The solid electrolyte interphase (SEI) formed by the reduction of electrolyte during the first charge has a major influence on the battery performance. The composition and morphology of the SEI depend on the type of electrolyte used and the impurities that are present. An understanding of the SEI formation mechanism may help identify a viable approach to control SEI composition and the consequent performance of the battery. FTIR analysis can provide information about the chemical structure of the surface layer. By combining FTIR results with DFT calculations, we gain insight into the SEI formation mechanism; we can exploit this to improve battery performance. This paper illustrates the power of combining experimental and theoretical analyses for studying the SEI formation mechanism, by using an investigation into the effect of trace amounts of oxygen on PC reduction as an example.

* Corresponding author.

E-mail address: sdlin@mail.ntust.edu.tw (S.D. Lin).

Among the wide range of polar solvents that are available, PC have attracted lots of research attention because of its remarkable ability to dissolve and dissociate lithium salts and provide electrolytes with high ionic conductivity over a wide temperature range [2,3]. Although PC is unsuitable for use as a single solvent, because of its tendency toward co-intercalation with lithium ion into graphite which causes exfoliation of graphite electrode, it can be used in conjunction with other cyclic and acyclic carbonates, such as EC and DMC [4], or with electrolyte additives [5–9].

The presence of trace amounts of impurities, such as H_2O , O_2 , and CO_2 in the electrolyte, can affect the electrochemistry of non-aqueous systems, leading to the formation of Li_2CO_3 , Li_2O_2 , LiO_2 , and LiOH [10]. Water can degrade the commonly used LiPF_6 -based electrolytes, reducing the electrolyte's concentration, and can decompose some of the SEI's major components at a carbon anode [11,12]. The reduction of oxygen impurities may produce unwanted contaminants such as Li_2O_2 and LiO_2 [13,14], which consequently decrease battery performance. Aurbach et al. [13] suggested that oxygen reduction products might undergo chemical reaction with PC, although no detailed explanation was provided. To our knowledge, there are no reports of combined theoretical and experimental analyses on the reduction mechanisms of cyclic diesters of carbonic acids, such as propylene carbonate, in the presence of oxygen in lithium-ion batteries. However, there are some reports of mechanistic studies on the lithium air battery [14,15]. By combining theoretical and experimental methods, we determined the effect of oxygen on the reduction mechanism of PC, a cyclic diester of carbonic acids.

2. Experimental and calculations

PC (Aldrich, 99.7%) and LiPF_6 (Novolyte technologies) were used to prepare a 1.1 M LiPF_6/PC solution. To investigate the effect of oxygen impurities on the reduction of PC, we used electrolyte that had been degassed by purging with argon gas (99.99%) for 15 min, and compared the results with those for PC electrolyte that had not been degassed. Cyclic voltammetry (CV) and linear sweep voltammetry (LSV) measurements were made using a three-electrode Teflon cell with type 304 stainless steel working and counter electrodes (Yang Cheng Packing Co., area 1 cm^2), and a lithium reference electrode, using a VMP3 multi-channel potentiostat (Bio Logic Science Instruments) at a scan rate of 0.1 mV s^{-1} . Type 304 stainless steel was chosen as a working electrode similar to the previous studies by Meitav et al. [16] and Wang et al. [17] because of its compatibility and inert behavior in the system used and its inexpensiveness. Prior to each measurement, the stainless steel electrodes were polished with $0.05 \mu\text{m}$ colloidal silica and kept in vacuum overnight.

For FTIR measurements, we used an FTIR spectrometer (Bruker Optics) equipped with a single-reflection attenuated total reflectance (ATR) sampling accessory. After careful adjustment of the electrode position to provide the maximum intensity, each spectrum was recorded by accumulating 128 scans with a resolution of 4 cm^{-1} . FTIR measurements using the stainless steel electrode were conducted at OCV (approximately 3 V), 2.5 V, 1.6 V, and -0.1 V for the untreated solution, and at OCV (approximately 3 V), 1.6 V, and -0.1 V for the argon-purged solution. After conducting LSV from OCV to the target potential, the electrode was washed with dimethyl carbonate (DMC, Aldrich) for 60 s, dried in a vacuum chamber for 1 h, and then used to obtain the FTIR spectrum. To identify the reduction products formed at each potential range, we made subtraction between two successive IR spectra using the PC ring stretching absorption band at 1355 cm^{-1} to determine the correct subtraction parameter. The subtraction for the non-purged electrolyte was done between the spectra at 2.5 V and 1.6 V, and

between 1.6 and -0.1 V ; whereas, for the degassed electrolyte, the subtraction was performed between the spectra at OCV and 1.6 V, and between 1.6 and -0.1 V . All electrolyte preparations, degassing, electrochemical measurements, and FTIR measurements were performed inside an argon-filled glove box (H_2O and $\text{O}_2 < 1 \text{ ppm}$) at room temperature.

XPS measurements were performed by using a VG ESCA Scientific Theta Probe spectrometer, using the Al K-alpha line ($\text{h}\nu = 1486.7 \text{ eV}$). Samples were transferred to the XPS spectrometer inside an argon-filled sample box. The carbon 1s peak at 285 eV was used as the binding energy scale reference, and the Ag 3d_{5/2} line at 368 eV with full width at half maximum (FWHM) of 0.66 eV was used to calibrate the spectrometer. High-resolution spectra were acquired using a constant pass energy of 50 eV, and the pressure in the analysis chamber was maintained at roughly $6 \times 10^{-9} \text{ mbar}$. Data analyses were performed using Gaussian–Lorentzian curve fitting with Shirley background subtraction.

All geometry optimizations and frequency determinations were performed using the Gaussian 09 package [18]. We applied density functional theory (DFT) because of its favorable balance between accuracy and computational efficiency. We used B3LYP, a widely used hybrid functional comprising the Becke's three-parameters, the exact exchange functional (B3), and the non-local gradient corrected correlation functional of Lee–Yang–Parr (LYP) [19–22], with the triple split valence basis set 6-311G and a set of d,p polarization functions for heavy atoms and hydrogen atoms [23]. A spin-unrestricted scheme was applied for odd-numbered electron systems to allow for any possible bond cleavage during geometry optimization.

To confirm the transition states and to make zero point energy (ZPE) corrections, we conducted frequency analyses using the same basis set we employed for geometry optimization. Intrinsic reaction coordinate (IRC) calculations were performed to confirm whether the reaction path of a given chemical reaction correctly connected the stationary points under consideration. Unless otherwise stated, the relative energies indicate those with ZPE correction, and Gibbs free energies and enthalpies are calculated at 298.15 K. Spin contamination was considered by comparison of the expectation value of the $\langle S^2 \rangle$ operator. Before annihilation, $\langle S^2 \rangle$ was mainly between 0.75 and 0.77 for doublet states, confirming that spin contamination would have an insignificant effect on the calculation result. Natural Bond orbital (NBO) [24] analysis was performed with the NBO program included in the Gaussian program package, using the same basis set used for geometry optimization.

Implicit solvent effects were accounted for by applying the implicit Solvation Model with Density (SMD) method [25] as implemented in Gaussian 09; a PC dielectric constant of 64.9 was chosen to reflect the conditions implemented in the experiments. Vibrational frequencies were calculated at the same levels of theory used for characterization of stationary points and for the simulations of vibrational spectra. Vibrational frequency calculations performed at DFT contain known error because of anharmonicity; thus, a scaling factor of 0.963 was applied for B3LYP/6-311++G(d,p) to match the calculated frequency values with those obtained from the experimental spectra. For all simulated vibrational spectra, we used 50% Gaussian and 50% Lorentzian functions with an FWHM of 20 cm^{-1} .

3. Result and discussion

3.1. Cyclic voltammetry measurements

Fig. 1 shows the cyclic voltammogram for a stainless steel electrode in the 1.1 M LiPF_6/PC solution with and without electrolyte purging. Three main reduction peaks at 2.3 V with a shoulder at 1.9 V, a broad peak between 1.5 and 0.9 V, and a peak at 0.6 V are

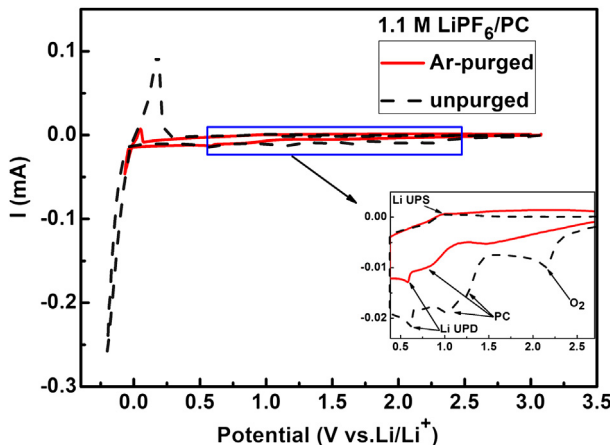


Fig. 1. Cyclic voltammogram of stainless steel electrode in 1.1 M of LiPF₆/PC with (solid line) and without (dash line) purging with argon gas. The inset shows the enlarged part of the region between 0.4 V and 2.7 V.

observed in the cyclic voltammogram of non-purged solution (Fig. 1, dash line). The cathodic peak at 2.3 V with a shoulder at 1.9 V is attributed to the reduction of oxygen [13], indicating the presence of oxygen impurities in the electrolyte. To examine the behavior of this peak, we performed CV analysis in the region between OCV to 1.6 V, and the corresponding cyclic voltammogram is shown in Fig. 2. The irreversible reduction peaks at 2.3 V and 1.9 V are absent in the second and subsequent cycles, suggesting either that the trace amount of oxygen was completely reduced or that a passive film formed on the electrode surface and inhibited further reduction of oxygen.

We assigned the broad reduction peak in the region between 1.5 and 0.9 V to the reduction of PC. Zhang et al. observed the reduction of PC in the range 1.0–1.6 V on a gold electrode, and reported that a shallow and broad feature in the voltammogram was due to the slow reduction kinetics of PC, making it impossible to assign a precise value to the reduction potential [26]. Similar PC reduction trends were observed on Pt [27], Ni [28], and Au [13] electrodes. The broad reduction wave observed in our experiment split into a clearly resolved peak centered at 1 V and a shoulder at 1.2 V, suggesting the occurrence of two film-forming processes at the stainless steel electrode. We attributed the cathodic peak at 0.6 V

with a corresponding anodic feature at 0.98 V to Li under potential deposition (UPD) [13,26,29] on the stainless steel electrode. These peaks are similar to the observation made by Myung et al. [30] for a stainless steel electrode, with a cathodic peak at 0.5–0.7 V and an anodic peak at 1.1–1.3 V.

For comparison, CV analysis of the purged 1.1 M LiPF₆/PC solution (Fig. 1, solid line) revealed some pronounced reduction peaks. The oxygen reduction peaks at 2.3 V and 1.9 V was significantly diminished in the CV using the purged electrolyte (Fig. 1, solid line), indicating that the degassing process was effective in the removal of dissolved oxygen. Although the figure shows a smaller cathodic current, the reduction of PC is observed as a broad peak in the potential region 1.1–0.7 V. The coupled redox peaks at 0.58 and 0.9 V, because of Li UPD on the stainless steel electrode, were also present.

The dissolution of the components, such as Cr, Ni, and Fe, of type 304 stainless steel was not observed in the potential region we scanned. If the components of the stainless steel interfered in the SEI formation, this behavior should be observed in both the CV of the degassed and the non-degassed electrolyte. However, the PC reduction in the absence of trace oxygen in Fig. 1 (solid line) was similar with that reported over Au, Ag, and Ni electrode [13,28]. Therefore, the changes in reduction in the non-degassed are assigned to the influence of oxygen. On the other hand, if the dissolution of these metal components occurred in the CV potential region, we should observe the respective oxidation peaks during the anodic polarization [30]. However, this was not observed in the CV of both for the non-degassed and degassed electrolytes Furthermore, the formation of alloy with lithium metal was not observed near 0 V vs Li/Li⁺ in Fig. 1 (both solid and dash lines).

3.2. Li⁺ solvation in PC-based electrolyte solutions

Decomposition reactions in lithium-ion batteries are strongly affected by lithium-ion solvation; thus, it is reasonable to consider the solvation of lithium ions in the electrolyte solution using DFT calculations. Table 1 shows a summary of the charges on lithium ions, the average Li⁺-O bond distance, binding energy per species, Gibbs free energy, heat of formation, and entropy changes for a system of Li⁺(PC)_n ($n = 0$ –4) supermolecular clusters calculated at the SMD/B3LYP/6–311++G(d,p) level. The average bond distance between lithium and oxygen increases with increasing numbers of solvating PC molecules, as shown in Table 1. The observed increase in bond length, which is in agreement with the gas phase calculation results reported by Wang et al. [31], is accompanied by a decrease in binding energy, probably because of repulsion between coordinated molecules. Furthermore, the positive charge on lithium ion decreases with increasing n . We attributed this observation to the wider distribution of the positive charge of lithium in space as the size of the solvated lithium ion increases.

The entropy changes listed in Table 1 include entropy changes for both the system and the surrounding; the surrounding gains

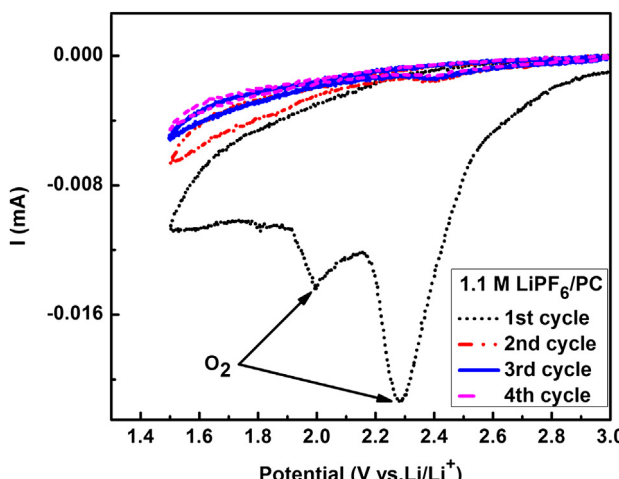


Fig. 2. Cyclic voltammogram of stainless steel electrode in 1.1 M of LiPF₆/PC without purging with argon gas in the higher potential region where only reduction of oxygen was observed.

Table 1

The charges on lithium ions (q), the average Li⁺-O distance (r , Å), binding energies (BE, kcal mol⁻¹), heat of reaction (ΔH , kcal mol⁻¹), Gibbs free energies of the reaction (ΔG , kcal mol⁻¹) and the total entropy change (ΔS , kcal mol⁻¹ K⁻¹) at 298.15 K calculated at the SMD/B3LYP/6–311++G(d,p) level.

Reactions	q	r	BE ^a	ΔH^b	ΔG^c	ΔS^d
Li ⁺ + PC → Li ⁺ (PC)	0.991	1.90	23.22	-67.77	-40.79	0.137
Li ⁺ (PC) + PC → Li ⁺ (PC) ₂	0.966	1.91	21.34	-43.93	-26.98	0.090
Li ⁺ (PC) ₂ + PC → Li ⁺ (PC) ₃	0.926	1.93	18.83	-25.1	-7.53	0.025
Li ⁺ (PC) ₃ + PC → Li ⁺ (PC) ₄	0.891	1.98	16.9	-12.55	2.64	-9 × 10 ⁻³

^a BE = $-\{E(Li^+(S)_n) - nE(S) - E(Li^+)\}/n$.

^b $\Delta H = H(Li^+(S)_n) - H(Li^+(S)_{n-1}) - H(S)$.

^c $\Delta G = G(Li^+(S)_n) - G(Li^+(S)_{n-1}) - G(S)$.

^d $\Delta S_{\text{total}} = \Delta S_{\text{system}} + \Delta S_{\text{surroundings}}$; where, $\Delta S_{\text{surroundings}} = -\Delta H/T$.

entropy because of the exothermic solvation reactions. Table 1 shows that the total entropy change during formation of $\text{Li}^+(\text{PC})_4$ is -9×10^{-3} kcal mol $^{-1}$ K $^{-1}$. Thus, the formation of $\text{Li}^+(\text{PC})_4$ is unfeasible because this would violate the Second Law of Thermodynamics. The $\Delta S_{\text{surroundings}}$ and ΔS_{total} values for the formation of $\text{Li}^+(\text{PC})_3$ were calculated as 0.084 and 0.025 kcal mol $^{-1}$ K $^{-1}$, respectively, confirming the thermodynamic favorability for the formation of $\text{Li}^+(\text{PC})_3$. The relative stability of $\text{Li}^+(\text{PC})_3$ compared to $\text{Li}^+(\text{PC})_4$ may also result from the potential gradient (electrostatic field) present in an electrochemical reaction. The structure of $\text{Li}^+(\text{PC})_3$ was found to be nearly planar, with a permanent dipole moment of 11.25 D in a direction perpendicular to the plane, whereas $\text{Li}^+(\text{PC})_4$ has a tetrahedral structure with a small dipole moment of 1.72 D. Hence, the greater likelihood of $\text{Li}^+(\text{PC})_3$ being aligned with the potential gradient may contribute to its greater stability compared to that of $\text{Li}^+(\text{PC})_4$.

Based on the preceding discussion, and from the calculated Gibbs free energies of formation for $\text{Li}^+(\text{PC})_n$ ($n = 0–4$), we propose that a maximum of three PC molecules can solvate a Li^+ ion in a PC-based electrolyte system. Wang et al. [31] suggested that the formation of a four-coordinated Li^+ species was unfavorable for PC-containing electrolyte systems. Electrospray ionization mass spectroscopy (ESI-MS) studies by Fukushima et al. [32–34] also support this conclusion. It is understandable that the solvation number of Li^+ is partly dependent on the steric effects of the respective solvent molecules. For example, favorable Li^+ solvation numbers, as determined by Fourier transform ion cyclotron resonance spectrometry, are reported to be two in diethyl ether, and three in acetone and tetrahydrofuran [35].

3.3. Decomposition mechanism of PC in the presence of oxygen

The electrochemical reduction of oxygen to form the superoxide ion can occur after gaining an electron from the negatively polarized electrode. Previous electrochemical studies on oxygen reduction in organic solvents demonstrate that it is possible to reduce molecular oxygen to superoxide anion (O_2^-) in a non-aqueous environment [36–39]. Formation of the superoxide anion, which is a free radical, can be taken advantage of because it can behave as a Lewis base or a nucleophile, and as either an oxidizing or a reducing agent. Pearson's Hard Soft Acid Base (HSAB) theory, combined with the relative stabilities of $\text{Li}^+(\text{PC})_n$ complexes, can account for the possible O_2 reduction products formed in the PC-based electrolyte solutions. As demonstrated by our cyclic voltammetry experiments, oxygen undergoes reduction to yield a superoxide radical, O_2^- , which is the species responsible for subsequent decomposition reactions. Based on HSAB theory, superoxide is a moderately soft base with low affinity for Li^+ , a hard acid. Hence, the superoxide formed as the first O_2 reduction product most favorably undergoes an $\text{S}_{\text{N}}2$ type reaction with PC.

Based on our calculations, the superoxide radical undergoes a nucleophilic attack at the CH_2 group of PC, resulting in a heterolytic ring-opening reaction. This reaction proceeds through a transition state, **2**, with a ring-opening barrier of 6.28 kcal mol $^{-1}$, and yields the peroxoradical species, **3**. Concerning the reactivity of superoxide toward esters, previously reported experimental and DFT studies also proposed a nucleophilic attack at the CH_2 group through a $\text{S}_{\text{N}}2$ type mechanism, which is much more favorable than an attack at the carbonyl carbon or at the relatively hindered CH group [40,41]. The peroxoradical then passes through a transition state, **4**, with a relatively high-energy barrier of 46.43 kcal mol $^{-1}$, to undergo homolytic bond cleavage at the O–O bond and form a stable primary radical. The DFT-calculated potential energy and Gibbs free energy profiles for the PC decomposition mechanism in the presence of superoxide radical are shown in Fig. 3 and Table 2.

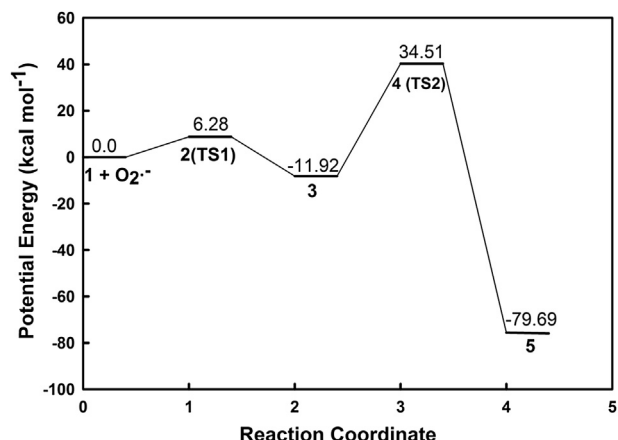


Fig. 3. Potential energy profile for the reductive decomposition mechanism of $\text{Li}^+(\text{PC})_3$ assisted by superoxide radical calculated with DFT method.

Fig. 4 shows the complete proposed reduction mechanism, as determined from our calculations. There is a possibility of further reduction of the primary radical by gaining electron from the polarized stainless steel electrode. The resulting reactive carbanion, **6**, may undergo a barrierless ion-pairing reaction with either Li^+ or $\text{Li}^+(\text{PC})_3$ to generate **7** and **8**, respectively. The change in Gibbs free energy (ΔG) for these ion-pairing reactions was calculated to be greater for the generation of **8** compared to that for the formation of **7** (-112.32 vs. -91.62 kcal mol $^{-1}$), indicating the favorable formation of **8**. The calculated vibrational frequency for **8** gives a realistic reproduction of both band intensity distribution and general spectral features, compared to the FTIR measurement at 1.6 V (see Section 3.5).

3.4. Reductive decomposition mechanism of $\text{Li}^+(\text{PC})_3$

We investigated the possible $\text{Li}^+(\text{PC})_3$ electroreduction mechanisms and the major solvated species in PC-based electrolytes, in the absence of oxygen. The potential energy and Gibbs free energy profile for reductive dissociation of $\text{Li}^+(\text{PC})_3$ in solution are shown in Fig. 5, the relative potential energies and Gibbs free energies are listed in Table 3, and our proposed mechanism is shown in Fig. 6. Since the LUMO of $\text{Li}^+(\text{PC})_3$ lies on the ethereal C–O bond, upon addition of an electron, the C–O antibonding orbitals are occupied, facilitating bond stretching leading to barrierless ring-opening of the PC moiety. This finding is consistent with our NBO analysis, which revealed spin density coefficient of 0.58 for oxygen, indicating that the additional electron is mainly located on the oxygen atom of the reduced species **10**. Inner-sphere electron transfer processes facilitate the conversion of **10** through transition state **11**, with a relatively low energy barrier of 9.96 kcal mol $^{-1}$, to

Table 2

Relative energies, enthalpies and free energies (in kcal mol $^{-1}$) of the stationary points, and imaginary frequency (ω/cm^{-1}) for the decomposition mechanism of PC in the presence of superoxide radical calculated with SMD-B3LYP/6-311++G(d,p).

Structures	$\Delta E + \Delta ZPE$	ΔH	ΔG	ω
1	0.0	0.0	0.0	
2 (TS, $1 \leftrightarrow 3$)	6.28	12.55	14.43	211 <i>i</i>
3	-11.92	-13.18	-7.53	
4 (TS, $3 \leftrightarrow 5$)	34.51	28.83	40.79	61 <i>i</i>
5	-79.69	-80.32	-83.46	
6	-109.81	-109.82	-109.19	
7	-99.77	-100.40	-91.62	
8	-127.20	-120.48	-112.32	

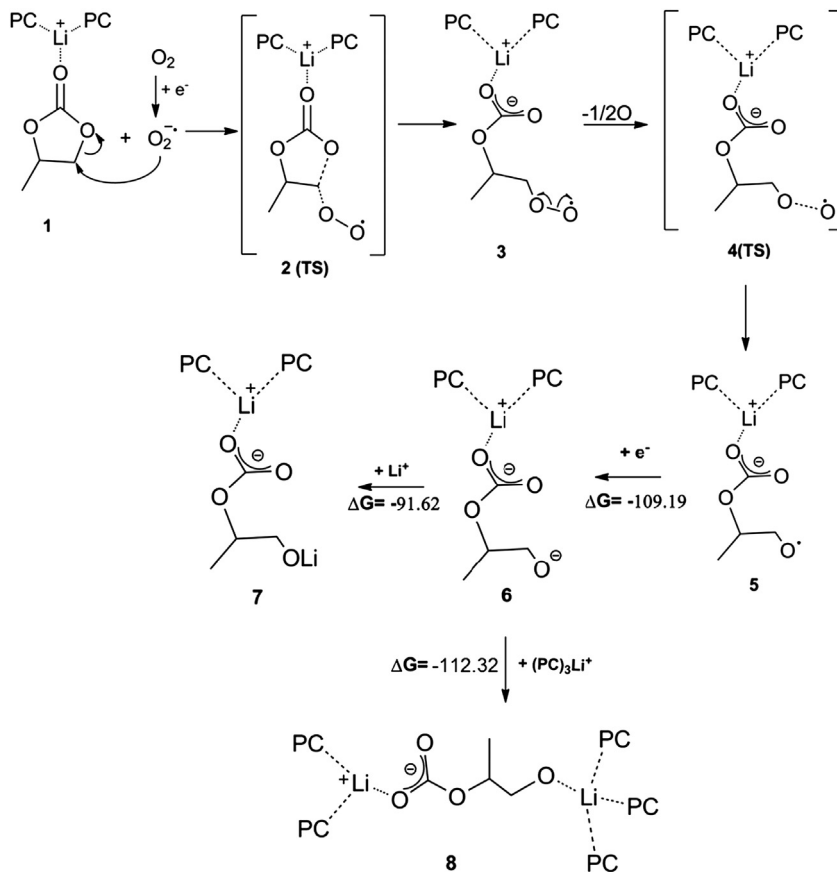


Fig. 4. The reductive decomposition mechanism of PC in the presence of superoxide radical, values are given in kcal mol^{-1} .

the primary radical intermediate **12**. The unpaired electron in **12** is shifted from the ethereal oxygen onto the terminal carbon, with an occupancy coefficient of 0.99. The primary radical then undergoes a barrierless homocoupling or dimerization reaction, to give $(\text{R}-\text{OCO}_2-\text{Li})_2$, **15**. This is one of the possible reduction products of $\text{Li}^+(\text{PC})_3$, as indicated by the Gibbs free energy for the reaction ($\Delta G = -144.96 \text{ kcal mol}^{-1}$). There is a possibility of further reduction of the primary radical, by gaining an electron from the polarized electrode to generate $(\text{PC})_2-\text{LiCO}_3$, **13**, which can react with another $\text{Li}^+(\text{PC})_3$ in solution to produce propylene gas and Li_2CO_3 solvated by four PC molecules, **14**. Assuming that **14** and **15**

are among the major reduction products of $\text{Li}^+(\text{PC})_3$, the calculated vibrational frequencies of the molecules give a good reproduction of the observed FTIR spectral features measured at -0.1 V (see Section 3.5).

3.5. FTIR measurements

FTIR analysis was performed inside a glove box at various potentials for both the degassed and non-purged electrolyte solutions; subtraction between the successive IR spectra was made to determine the products formed at different potentials. Fig. 7 shows the calculated spectrum for $\text{Li}^+(\text{PC})_3$ and the experimental FTIR spectrum for non-purged 1.1 M LiPF_6/PC over a stainless steel electrode at OCV (3.15 V vs. Li/Li^+). The experimental and calculated vibrational modes show good agreement, and the observed absorption peaks are consistent with previous reports [42]. Absorption bands caused by C=O stretching vibrations are present at 1787

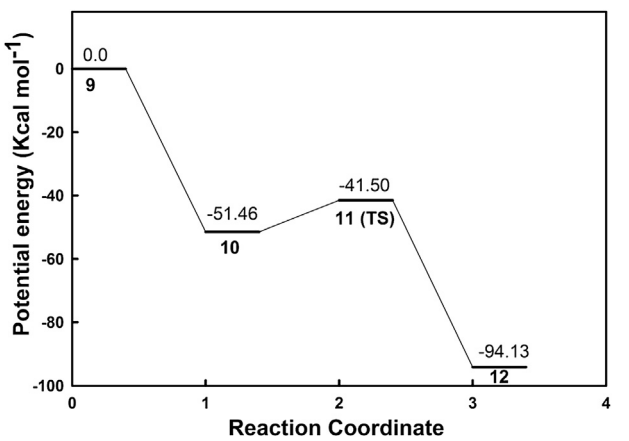


Fig. 5. Potential energy profile for the reductive decomposition mechanism of $\text{Li}^+(\text{PC})_3$.

Table 3

Relative energies, enthalpies and free energies (in kcal mol^{-1}) of the stationary points, and imaginary frequency (ω/cm^{-1}) for the decomposition mechanism of $\text{Li}^+(\text{PC})_3$ calculated with SMD-B3LYP/6-311++G(d,p).

Structures	$\Delta E + \Delta ZPE$	ΔH	ΔG	ω
9	0.0	0.0	0.0	
10	-51.46	-50.32	-49.57	
11(TS, 10 ↔ 12)	-41.50	-40.50	-38.64	900i
12	-94.13	-78.44	-92.24	
13	-48.98	-48.94	-50.20	
14	-151.23	-136.17	-135.54	
15	-163.15	-149.35	-144.96	

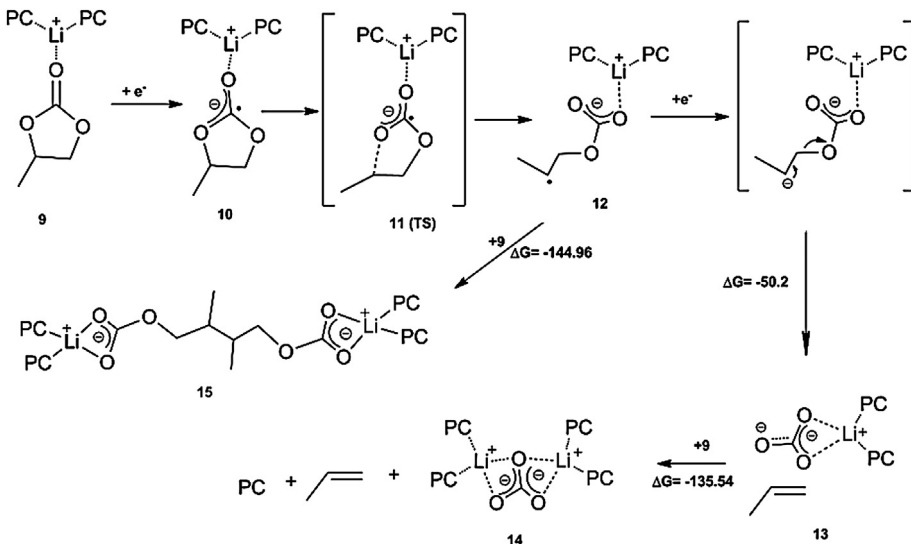


Fig. 6. The reductive decomposition mechanism of $\text{Li}^+(\text{PC})_3$, values are given in kcal mol^{-1} .

and 1772 cm^{-1} . The absorption bands at 2990 and 2938 cm^{-1} are the C–H stretching modes of the CH_3 and CH_2 groups, whereas those at 1484 , 1452 , and 1389 cm^{-1} are assigned to the respective twisting, scissoring, and wagging vibrations of CH_3 and CH_2 . Asymmetric stretching and bending absorptions of the $-\text{CO}_2$ group coordinating to the lithium cation are observed at 1183 , 1119 , 777 , 713 cm^{-1} . Table 4 lists the band assignments based on literature [42–47] and those from our DFT calculations. The slight disagreement in the C–H vibration regions may be resulted from the influence of the solid phase surrounding.

Fig. 8 shows the subtractive spectrum obtained using a stainless steel electrode at various potentials. In the subtractive spectrum, the FTIR spectrum obtained at OCV was subtracted from the spectrum taken at 2.5 V , and the spectrum taken at 2.5 V was subtracted from the 1.6 V spectrum. The FTIR spectral features at 2.5 V and 1.6 V , shown in Fig. 8a and b, are similar, with only a $\pm 2 \text{ cm}^{-1}$ peak shift observed for some peaks. A possible explanation for the presence of similar features in these regions is that oxygen reduction began at 2.5 V and ended at 1.6 V , as is apparent from the cyclic

voltammogram (Fig. 1). Hence, we assume that the reduction products formed in these potential regions are the same with the greater amount of product formed at 1.6 V ; this is supported by the more intense peaks in the 1.6 V spectrum compared to those of the 2.5 V spectrum. The major band assignments, based on the 1.6 V spectrum the region where the oxygen reduction is completed, are shown in Table 5.

Bands appearing at 2964 , 2858 , 1676 , 1312 , 1124 , and 1074 cm^{-1} in the 1.6 V spectrum (Fig. 8b) indicate the formation of $(\text{PC})_2\text{LiOC(O)OCH}(\text{CH}_3)\text{CH}_2\text{OLi}(\text{PC})$ (8). Such species are less cohesive and adhesive since they are rich in methyl groups. Hence, the formation of this passivating surface film requires an intensive reduction of solution species, and accompanied by the formation of propylene gas [48]. The absorption bands appearing at 2929 , 1775 , 1727 , 1269 , 1210 , 960 , and 786 cm^{-1} result from various vibration modes of solvated PC. Compared to the corresponding FTIR peaks at OCV, these peaks exhibit a significant shift in wavenumber because of solvation effects.

Fig. 8c shows a subtractive FTIR spectrum obtained by subtracting the 1.6 V spectrum from the -0.1 V spectrum. Since the bands due to the oxygen reduction products are subtracted, we only expect to see bands representing the PC reduction products in the

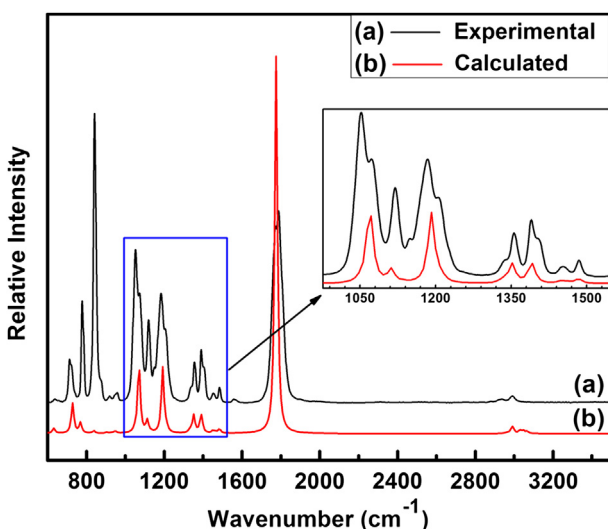


Fig. 7. Comparison of the FTIR spectra of $1.1 \text{ M LiPF}_6/\text{PC}$ from stainless steel electrode at OCV (a) and DFT-calculated spectrum (b).

Table 4

FTIR vibrational frequency taken at OCV for $1.1 \text{ M LiPF}_6/\text{PC}$ and calculated for $\text{Li}^+(\text{PC})_3$ with SMD-B3LYP/6-311++G(d,p) and band assignments.^a

Assignment	Observed (cm^{-1})	Calculated (cm^{-1})
$\nu_s \text{ CH}_3$	2990, 2938	2993
$\nu_{\text{C=O}}$	1787, 1772	1775
$\tau \text{ CH}_2 + \zeta \text{ CH}_2$	1484	1484
$\zeta \text{ CH}_3$	1452	1459, 1448
$\omega \text{ CH}_2, \omega \text{ O–CH}_2$	1389	1387
$\nu_{\text{Ring}}, \omega \text{ CH}_2$	1355	1352
$\nu_{\text{as}} (\text{O–C=O}), \nu_s (\text{C=O–C}), \omega \text{ CH}_2$	1183	1189
$\nu_s \text{ CH}_2\text{–CH–CH}_3$	1119	1112
$\nu_{\text{Ring}}, \nu_s \text{ C–O}$	1072,	1072
$\nu_s (\text{C–CH}_3)$	1052	1049
$\nu_s \text{ C–C}$	957	948
P–F of LiPF_6	840	–
$\nu_{\text{as}} (\text{O–C=O}), \text{Ring deformation}$	777	768
O–C=O (asymmetric bending)	713	723

^a ν , stretching, ν_s , symmetric stretching, ν_{as} , asymmetric stretching, τ , twisting, ζ , scissoring, ω , wagging.

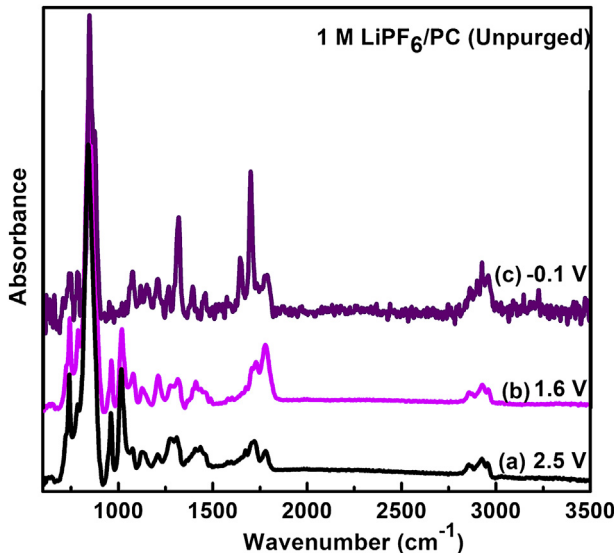


Fig. 8. The subtractive FTIR spectra from not-purged 1.1 M LiPF₆/PC: (a) 2.5 V – OCV, (b) 1.6 V to 2.5 V, and (c) –0.1 V to 1.6 V.

figure. Various works reported the PC reduction mechanism and products on different electrodes [29,49–51]. Zhuang et al. suggested the direct formation of lithium carbonate and propylene gas by the reduction of co-intercalated PC via two electron reductive pathways, based on their DFT calculation and FTIR results [50]. Conversely, Aurbach et al. reported that the main reduction product of PC on lithium metal electrode is a bifunctional derivative of propylene carbonate with the evolution of propylene gas, rather than direct formation of Li₂CO₃ through two electron transfers per PC molecule [29,51]. They explained that the formation of Li₂CO₃ occurred as the main product because of the reaction of lithium alkyl carbonate with trace amounts of water, or by the continued reduction of lithium alkyl carbonate. A further report suggested that PC may follow a single-electron reduction pathway on non-porous electrodes such as Ni [49]. Our DFT calculation and experimental result support the reduction of PC through a one-electron transfer, to yield the primary radical intermediate **12**, which either undergoes radical termination to form lithium alkyl dicarbonate, or undergoes further reduction to yield lithium carbonate with the evolution of propylene gas, as discussed in Section 3.4. The FTIR spectrum shown in Fig. 8c can be easily resolved into two

components, (ROCO₂Li)₂ and Li₂CO₃. The absorption bands observed at 2965–2990, 1701, 1648, 1320, 1297, 1117, and 1060 cm⁻¹ and the bands at 1575, 1058, and 875 cm⁻¹ are characteristic of lithium alkyl dicarbonate and lithium carbonate, respectively. Based on the DFT calculation, Li₂CO₃-(PC)₃ and (R-OCO₂-Li)₂ are among the major Li⁺-(PC)₃ reduction products. Hence, we were able to make the band assignments shown in Table 6 with the aid of the calculated vibrational frequencies of these molecules and previously reported data. All the products formed in our system (**8**, **15**, and **14**) are poor passivating films on the graphite surface because of the presence of extra methyl group, and hence, PC cannot be used as a single solvent for graphite electrodes. However, using EC as a co-solvent, graphite electrodes can be cycled several times in PC-based electrolytes. Aurbach et al. [48] reported that the surface film formed due to PC reduction contains a less passivating species, whereas the reduction products of EC can form a relatively more compact and stable film on the electrode surface. This is because of the less cohesive nature of the methyl groups found in the PC reduction products. A comparison study of PC and EC by Xu shows, both PC and EC follow a similar single reduction pathway, however, the bulk properties of their reduction products are different [49]. Moreover, Zhuang et al. [52] explained that the reduction products of EC are characterized by intermolecular associations while in the PC counterparts such interaction is weakened as a result of the presence of methyl rich species.

Fig. 9 shows the FTIR spectra of degassed 1.1 M LiPF₆/PC for various potential regions. Absorption bands marked with an asterisk indicates the peaks that come from the associated PC molecules that show a similar feature as the electrolyte peaks. The OCV FTIR spectrum was subtracted from the 1.6 V spectrum; similarly, the 1.6 V spectrum was subtracted from the –0.1 V spectrum. For comparison, the subtractive FTIR spectrum from the non-purged electrolytes is included in Fig. 9. The cyclic voltammogram for the degassed electrolyte (Fig. 1, solid line) does not feature a reduction peak in the potential region from OCV to 1.6 V. In accordance with this result, the 1.6 V spectrum is nearly identical to the OCV spectrum. The absorption bands detected from the non-purged electrolyte, caused by the formation of (PC)₂LiOC(O)OCH(CH₃)CH₂OLi(PC), are not present in the degassed electrolyte FTIR spectrum, which is consistent with the effect of the presence of trace amount of oxygen in the electrolyte. The FTIR difference spectra for the potential range from 1.6 V to –0.1 V for both solutions are virtually the same. This result indicates that the reduction of PC alone occurred at the stainless steel electrode, irrespective of the presence of oxygen, and yields (ROLi-CO₂Li)₂ and Li₂CO₃ products.

3.6. XPS analysis

To support the FTIR results, after LSV, we performed XPS analysis of the electrode with the non-purged electrolyte, from OCV to 1.6 V, the oxygen reduction potential. Combining the information from these two techniques provides an understanding of the formation mechanism and morphology of the SEI. Fig. 10 shows the deconvoluted C 1s, F 1s, P 2p, O 1s, and Li 1s spectra of the stainless steel electrode after LSV measurement in the range from OCV to 1.6 V.

3.6.1. C 1s spectra

The C 1s spectrum of the stainless steel electrode at 1.6 V is shown in Fig. 10a. Three main peaks appear at 285.0, 286.65, and 288.75 eV. We attributed the peak at 285.0 eV to carbon atoms bound only to C or H atoms, and to hydrocarbon contaminants usually found in the XPS chamber. The peak at 286.65 eV resulted from carbon atoms bound to one oxygen atom (–C–O or -C=O–CO₂), and the peak at 288.75 eV is due to the carbon atom, bound to the three-oxygen atom (–OCO₂–). The peak intensity at

Table 5

FTIR vibrational frequency taken at 1.6 V for 1.1 M LiPF₆/PC and calculated for (PC)₂LiOC(O)OCH(CH₃)CH₂OLi(PC)₃ (**8**) with SMD-B3LYP/6-311++G(d,p) and band assignments.^a

Assignment	Observed (cm ⁻¹)	Calculated (cm ⁻¹)
v _S CH ₃ , v _S CH ₂ , v _S C–H, v _{as} CH ₃ ,	2964, 2929, 2858	3073, 2979, 2900
v _{C=O}	1775, 1727	1776, 1750
v _S (O–C–O)	1676	1613
ω CH ₂ + C–H bending	1406, 1434,	1409, 1436, 1396
τ CH ₃	1461, 1487	1446, 1484
v _S CO ₂ + τ CH ₂	1312	1307
τ CH ₂	1269	1266
v _S (O–C–O) + v _S (C–O–C)	1210, 1124,	1210, 1150
v _{Ring} + v _S (C–CH ₃)	1074	1076
v _S (C–O–C)	1017	1015
v _{as} C–C	960	961
P–F of LiPF ₆	840	—
v _{as} (O–C–O), Ring deformation	786	796

^a v, stretching, v_S, symmetric stretching, v_{as}, asymmetric stretching, τ, twisting, ζ, scissoring, ω, wagging.

Table 6

FTIR vibrational frequency taken at -0.1V for 1.1 M LiPF₆/PC and calculated for (Li₂CO₃-(PC)₃) (**14**) and (R-OOC₂-Li)₂ (**15**) with SMD-B3LYP/6-311++G(d,p) and band assignments.^a

Assignment	Observed (cm ⁻¹)	Calculated (cm ⁻¹) Li ₂ CO ₃ -(PC) ₃	Calculated (cm ⁻¹) (R-OOC ₂ -Li) ₂
v _S CH ₃ , v _S CH ₂ , v _S C-H, v _{as} CH ₃	2990, 2980, 2965, 2627, 2603	3050, 3043, 3008	3040, 2007, 2988, 2980
v _{C=O}	1790, 1701	1817, 1716	1793, 1773
v _S (O-C-O)	1648	—	1688
Li ₂ CO ₃	1575	1542	—
τ CH ₂ + ζ CH ₂	1450, 1395,	1430, 1389	—
τ CH ₂	1320, 1297	—	1309, 1294
v _S (O-C-O) + v _S (C-O-C)	1210, 1161, 1151,	1210, 1177, 1138	1216, 1209,
v _{Ring} + v _S (C-CH ₃)	1110, 1117	1096, 1094	1086, 1081
v _S (O-CH ₂)	1076, 1060	1079	1066
v _S C-O (Li ₂ CO ₃)	1058	1054	—
CO ₂ bending	875	868	—
P-F of LiPF ₆	840	—	—
v _{as} (O-C-O), Ring deformation	786	783	775

^a v, stretching; v_S, symmetric stretching; v_{as}, asymmetric stretching; τ , twisting; ζ , scissoring; ω , wagging.

286.65 eV is greater than that at 288.75 eV, suggesting that more than one carbon atom is bound to the oxygen atom [53–56]. This is possibly because of carbon atoms in (PC)₂LiOC(O)OCH(CH₃)CH₂OLi(PC) (**8**), in accordance with our DFT calculations and FTIR spectrum band assignments for this potential region.

3.6.2. O 1s spectra

The O 1s spectrum of the non-purged electrolyte (Fig. 10b) consists of four peaks that appear at 528.08, 530.33, 532.26, and 533.54 eV. The peak at 528.08 eV indicates the presence of small amount of Li₂O, which may have formed from the reaction of Lithium with oxygen that was generated as a byproduct during the

decomposition of PC in the presence of a superoxide radical (see Fig. 3). The peak at 530.30 eV corresponds to—C—O—Li, and was not resolved by FTIR analysis, whereas the peaks at 532.26 eV and 533.05 eV are attributed to ROCO₂Li and ROOC₂Li, respectively, in accordance with the C 1s spectrum [54,56]. Hence, the XPS result confirms the formation of (PC)₂LiOC(O)OCH(CH₃)CH₂OLi(PC) (**8**).

3.6.3. Li 1s spectra

The Li 1s spectra displayed in Fig. 10c show three peaks at 52.73, 54.98, and 56.63 eV. Both the—C—O—Li and —OOC₂—Li species show similar Li 1s spectra at 54.98 eV. We assigned the peak at 56.63 eV to the LiF, formed because of salt reduction [53,54,56]. The peak at

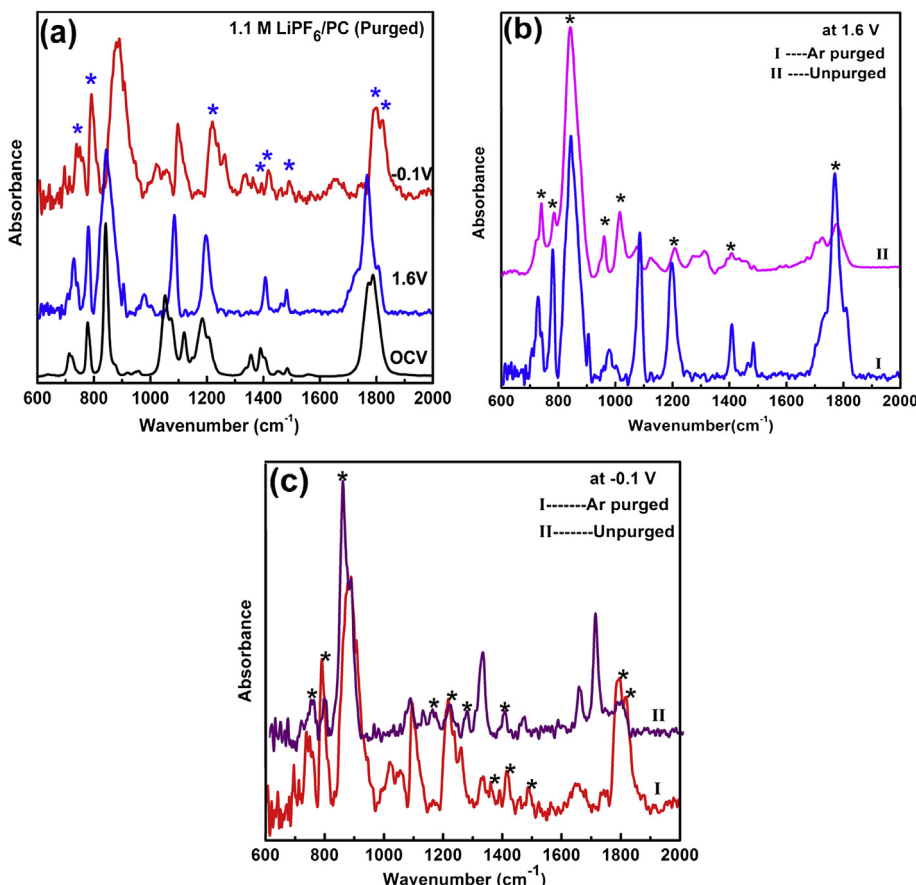


Fig. 9. The FTIR spectra of 1.1 M LiPF₆/PC (a) at OCV, 1.6 V (the subtractive spectrum between 1.6 V and OCV), and -0.1V (the subtractive spectrum between -0.1V and 1.6 V) from Ar-purged solution, (b) at 1.6 V with and without purging with argon and (c) at -0.1V with and without purging with argon.

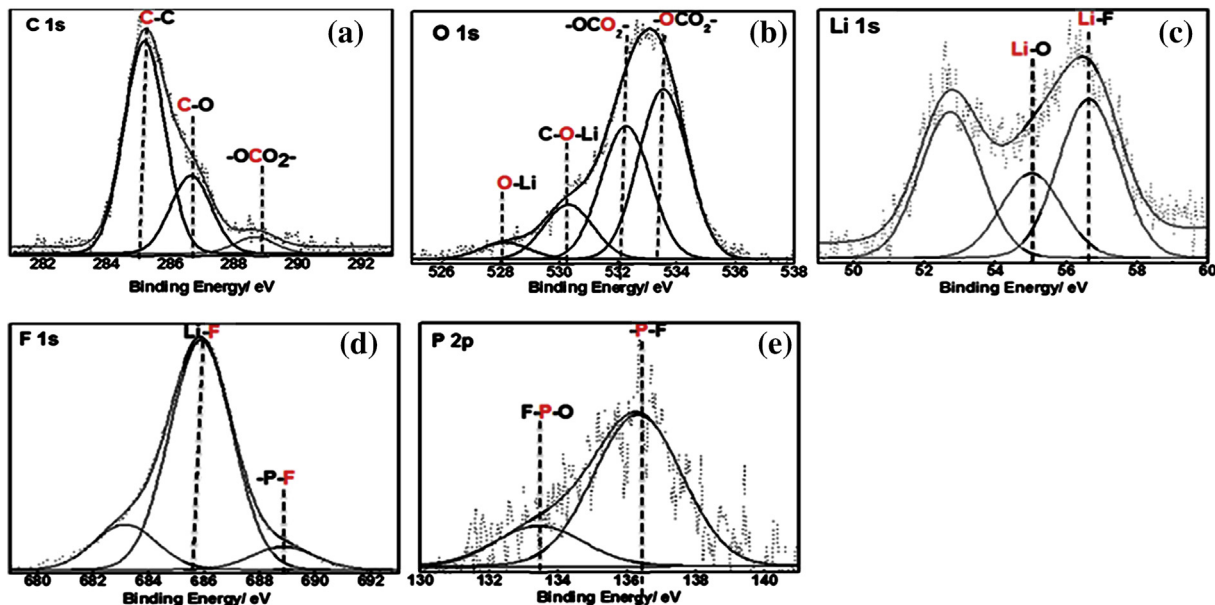


Fig. 10. C 1s (a), O 1s (b), Li 1s (c), F 1s (d) and P 2p (e) spectra of stainless steel electrode after LSV measurement from OCV to 1.6 V.

52.73 eV is in the region where Li metal is usually observed. However, we do not believe that the reduction of Li ion to Li metal occurs at this potential. Although the presence of unsolvated lithium salt and the possibility of interaction of lithium with the ethereal oxygen cannot be ruled out, we are unable to assign this peak at this moment.

3.6.4. F 1s and P 2p spectra

Fig. 10d shows the F 1s spectra of the non-purged electrolyte. Three peaks appear at 683.2, 685.9, and 688.95 eV. The peak at 685.9 eV is related to the formation of LiF because of salt reduction [57], and is in good agreement with the Li 1s spectra. We attributed the peak at 688.95 eV to a –P–F species, which indicates the presence of LiP_xF_y [56,58]. The peak observed at 683.2 eV is outside of the range where fluorine-containing lithium compounds are expected to appear, and thus, could not be assigned. Two asymmetric peaks, because of the presence of $2p_{3/2}$ and $2p_{1/2}$ doublets, at 136.3 and 133.8 eV, are present in the P 2p spectra (Fig. 10e). The peak at 136.3 eV confirms the presence of LiP_xF_y , and the small peak at 133.8 eV results from the occurrence of a small amount of Li_xPOF_y that is formed because of the presence of trace amounts of water, which is usually present in dipolar aprotic solvents [59,60].

4. Conclusion

We investigated the effect of the presence of oxygen on the reduction of propylene carbonate, which is among the most widely used solvents in lithium-ion batteries. We discussed the mechanistic aspects of SEI formation using both experimental and computational data. We found that the superoxide radical, which is an oxygen reduction product, decomposes PC through nucleophilic attack at the ethereal carbon atom, and generates a relatively stable primary radical that subsequently results in the generation of $(\text{PC})_2\text{LiOC(O)OCH}(\text{CH}_3)\text{CH}_2\text{OLi}(\text{PC})$. Although the reduction of PC follows the same process irrespective of the presence of oxygen, there is a possibility of an increase of surface film products through subsequent reactions of oxygen reduction. On the basis of the results presented here, we conclude that the major components of

the SEI in the current system are $(\text{PC})_2\text{LiOC(O)OCH}(\text{CH}_3)\text{CH}_2\text{OLi}(\text{PC})$, $\text{Li}_2\text{CO}_3\text{-}(\text{PC})_3$, $(\text{R}-\text{OCO}_2-\text{Li}(\text{PC}))_2$, where $\text{R} = -\text{CHCH}_2\text{CH}_3$, and Li_2O . However, most of these species are rich in methyl groups, which might render the species a poor passivating agent.

Acknowledgments

This work was supported by a grant from the Ministry of Economic Affairs of Taiwan, ROC (101-EC-17-A-08-S1-183). We are also grateful to the National Center of High-Performance Computing for computer time and facilities.

References

- [1] M. Morita, M. Ishikawa, Y. Matsuda, Organic electrolytes for rechargeable lithium ion batteries, in: Lithium Ion Batteries, Wiley-VCH Verlag GmbH, 2007, pp. 156–180.
- [2] M. Arakawa, J.I. Yamaki, J. Power Sources 54 (1995) 250–254.
- [3] K. Xu, Chem. Rev. 104 (2004) 4303–4418.
- [4] C. Wang, A.J. Appleby, F.E. Little, J. Electroanal. Chem. 519 (2002) 9–17.
- [5] C. Korepp, W. Kern, E.A. Lanzer, P.R. Raimann, J.O. Besenhard, M. Yang, K.C. Möller, D.T. Shieh, M. Winter, J. Power Sources 174 (2007) 628–631.
- [6] S.S. Zhang, J. Power Sources 162 (2006) 1379–1394.
- [7] R. Mogi, M. Inaba, S.-K. Jeong, Y. Iriyama, T. Abe, Z. Ogumi, J. Electrochem. Soc. 149 (2002) A1578–A1583.
- [8] W.-S. Kim, D.-W. Park, H.-J. Jung, Y.-K. Choi, Bull. Korean Chem. Soc. 27 (2006) 82–86.
- [9] E.G. Leggesse, J.-C. Jiang, RSC Adv. 2 (2012) 5439–5446.
- [10] G. Yosef, A. Doron, The electrochemical window of nonaqueous electrolyte solutions, in: Nonaqueous Electrochemistry, CRC Press, 1999.
- [11] Y. Wu, C. Jiang, C. Wan, E. Tsuchida, Electrochim. Commun. 2 (2000) 626–629.
- [12] T. Kawamura, S. Okada, J.-I. Yamaki, J. Power Sources 156 (2006) 547–554.
- [13] D. Aurbach, M. Daroux, P. Faguy, E. Yeager, J. Electroanal. Chem. Interfac. 297 (1991) 225–244.
- [14] Z. Peng, S.A. Freunberger, L.J. Hardwick, Y. Chen, V. Giordani, F. Bardé, P. Novák, D. Graham, J.-M. Tarascon, P.G. Bruce, Angew. Chem. Int. Ed. 50 (2011) 6351–6355.
- [15] T. Laino, A. Curioni, Chem. Eur. J. 18 (2012) 3510–3520.
- [16] A. Meitav, E. Peled, J. Electroanal. Chem. Interfac. 134 (1982) 49–63.
- [17] F.-M. Wang, H.-M. Cheng, H.-C. Wu, S.-Y. Chu, C.-S. Cheng, C.-R. Yang, Electrochim. Acta 54 (2009) 3344–3351.
- [18] M.J. Frisch, G.W. Trucks, H.B. Schlegel, G.E. Scuseria, M.A. Robb, J.R. Cheeseman, J. Montgomery, J. A., T. Vreven, K.N. Kudin, J.C. Burant, J.M. Millam, S.S. Iyengar, J. Tomasi, V. Barone, B. Mennucci, M. Cossi, G. Scalmani, N. Rega, G.A. Petersson, H. Nakatsuji, M. Hada, M. Ehara, K. Toyota, R. Fukuda, J. Hasegawa, M. Ishida, T. Nakajima, Y. Honda, O. Kitao, M. Klene, X. Li, J.E. Knox,

H.P. Hratchian, J.B. Cross, V. Bakken, C. Adamo, J. Jaramillo, R. Gomperts, R.E. Stratmann, O. Yazyev, A.J. Austin, R. Cammi, C. Pomelli, J.W. Ochterski, P.Y. Ayala, K. Morokuma, G.A. Voth, P. Salvador, J.J. Dannenberg, V.G. Zakrzewski, S. Dapprich, A.D. Daniels, M.C. Strain, O. Farkas, D.K. Malick, A.D. Rabuck, K. Raghavachari, J.B. Foresman, J.V. Ortiz, Q. Cui, A.G. Baboul, S. Clifford, J. Cioslowski, B.B. Stefanov, G. Liu, A. Liashenko, P. Piskorz, I. Komaromi, R.L. Martin, D.J. Fox, in: Gaussian, Inc., Wallingford CT, 2009.

[19] C. Lee, W. Yang, R.G. Parr, *Phys. Rev. B* 37 (1988) 785–789.

[20] A.D. Becke, *J. Chem. Phys.* 98 (1993) 5648.

[21] P.J. Stephens, F.J. Devlin, C.F. Chabalowski, M.J. Frisch, *J. Phys. Chem.* 98 (1994) 11623–11627.

[22] L.W.S.H. Vosko, M. Nusair, *Can. J. Phys.* 58 (1980) 1200–1211.

[23] M.J. Frisch, J.A. Pople, J.S. Binkley, *J. Chem. Phys.* 80 (1984) 3265–3269.

[24] A.E.R. E. D. Glendening, J. E. Carpenter, and F. Weinhold., NBO Version 3.1.

[25] A.V. Marenich, C.J. Cramer, D.G. Truhlar, *J. Phys. Chem. B* 113 (2009) 6378–6396.

[26] X. Zhang, R. Kostecki, T.J. Richardson, J.K. Pugh, J. Philip, N. Ross, *J. Electrochem. Soc.* 148 (2001) A1341–A1345.

[27] S.A. Campbell, C. Bowes, R.S. McMillan, *J. Electroanal. Chem. Interfac.* 284 (1990) 195–204.

[28] D. Pletcher, J.F. Rohan, A.G. Ritchie, *Electrochim. Acta* 39 (1994) 1369–1376.

[29] D. Aurbach, H. Gottlieb, *Electrochim. Acta* 34 (1989) 141–156.

[30] S.-T. Myung, Y. Sasaki, T. Saito, Y.-K. Sun, H. Yashiro, *Electrochim. Acta* 54 (2009) 5804–5812.

[31] Y. Wang, P.B. Balbuena, *J. Phys. Chem. B* 106 (2002) 4486–4495.

[32] Y. Matsuda, T. Fukushima, H. Hashimoto, R. Arakawa, *J. Electrochem. Soc.* 149 (2002) A1045–A1048.

[33] T. Fukushima, Y. Matsuda, H. Hashimoto, R. Arakawa, *Electrochim. Solid-State Lett.* 4 (2001) A127–A128.

[34] T. Fukushima, Y. Matsuda, H. Hashimoto, R. Arakawa, *J. Power Sources* 110 (2002) 34–37.

[35] R.L. Jarek, T.D. Miles, M.L. Trester, S.C. Denson, S.K. Shin, *J. Phys. Chem. A* 104 (2000) 2230–2237.

[36] E.L. Johnson, K.H. Pool, R.E. Hamm, *Anal. Chem.* 38 (1966) 183–185.

[37] D.L. Maricle, W.G. Hodgson, *Anal. Chem.* 37 (1965) 1562–1565.

[38] Y. Chen, S.A. Freunberger, Z. Peng, F. Bardé, P.G. Bruce, *J. Am. Chem. Soc.* 134 (2012) 7952–7957.

[39] M.E. Peover, B.S. White, *Electrochim. Acta* 11 (1966) 1061–1067.

[40] J. San Filippo, L.J. Romano, C.-I. Chern, J.S. Valentine, *J. Org. Chem.* 41 (1976) 586–588.

[41] V.S. Bryantsev, M. Blanco, *J. Phys. Chem. Lett.* 2 (2011) 379–383.

[42] Y. Ikezawa, T. Ariga, *Electrochim. Acta* 52 (2007) 2710–2715.

[43] D. Aurbach, M.L. Daroux, P.W. Faguy, E. Yeager, *J. Electrochem. Soc.* 134 (1987) 1611–1620.

[44] Y. Cheng, G. Wang, M. Yan, Z. Jiang, *J. Solid State Electrochem.* 11 (2007) 310–316.

[45] D. Aurbach, O. Chusid, *J. Electrochem. Soc.* 140 (1993) L155–L157.

[46] K.-i. Morigaki, *J. Power Sources* 103 (2002) 253–264.

[47] S.I. Pyun, *Fresenius J. Anal. Chem.* 363 (1999) 38–45.

[48] D. Aurbach, E. Zinigrad, Y. Cohen, H. Teller, *Solid State Ionics* 148 (2002) 405–416.

[49] K. Xu, *J. Electrochem. Soc.* 156 (2009) A751–A755.

[50] G.V. Zhuang, H. Yang, B. Blizanac, J. Philip, N. Ross, *Electrochim. Solid-State Lett.* 8 (2005) A441–A445.

[51] D. Aurbach, A. Zaban, Y. Gofer, Y.E. Ely, I. Weissman, O. Chusid, O. Abramson, *J. Power Sources* 54 (1995) 76–84.

[52] G.V. Zhuang, K. Xu, H. Yang, T.R. Jow, P.N. Ross, *J. Phys. Chem. B* 109 (2005) 17567–17573.

[53] S. Leroy, F. Blanchard, R. Dedryvère, H. Martinez, B. Carré, D. Lemordant, D. Gonbeau, *Surf. Interface Anal.* 37 (2005) 773–781.

[54] A. Schechter, D. Aurbach, H. Cohen, *Langmuir* 15 (1999) 3334–3342.

[55] R. Dedryvère, H. Martinez, S. Leroy, D. Lemordant, F. Bonhomme, P. Biensan, D. Gonbeau, *J. Power Sources* 174 (2007) 462–468.

[56] P. Verma, P. Maire, P. Novák, *Electrochim. Acta* 55 (2010) 6332–6341.

[57] A.M. Andersson, D.P. Abraham, R. Haasch, S. MacLaren, J. Liu, K. Amine, *J. Electrochem. Soc.* 149 (2002) A1358–A1369.

[58] M. Lu, H. Cheng, Y. Yang, *Electrochim. Acta* 53 (2008) 3539–3546.

[59] L.E. Ouatani, R. Dedryvère, C. Siret, P. Biensan, S. Reynaud, P. Iratcabal, D. Gonbeau, *J. Electrochem. Soc.* 156 (2009) A103–A113.

[60] L. Yang, B.L. Lucht, *Electrochim. Solid-State Lett.* 12 (2009) A229–A231.